

Two formation channels of UCDs in Hickson Compact Groups [★]

C. Da Rocha^{1,2}, S. Mieske³, I. Y. Georgiev⁴, M. Hilker², B. L. Ziegler², and C. Mendes de Oliveira⁵

¹ Núcleo de Astrofísica Teórica, Universidade Cruzeiro do Sul, R. Galvão Bueno 868, 01506-000, São Paulo, SP, Brazil

² European-Southern Observatory, Karl-Schwarzschild Str. 2, 85748 Garching, Germany

³ European Southern Observatory, Alonso de Cordova 3107, Vitacura, Santiago, Chile

⁴ Argelander Institut für Astronomie, Universität Bonn, Auf dem Hügel 71, 53121 Bonn, Germany

⁵ Instituto de Astronomia, Geofísica e Ciências Atmosféricas, Universidade de São Paulo, Rua do Matão 1226, Cidade Universitária, 05508-900, São Paulo, SP, Brazil

ABSTRACT

Context. The formation of ultra-compact dwarf galaxies (UCDs) is believed to be interaction driven, and UCDs are abundant in the cores of galaxy clusters, environments that mark the end-point of galaxy evolution. Nothing is known about the properties of UCDs in compact groups of galaxies, environments where most of galaxy evolution and interaction is believed to occur and where UCDs in intermediate state of their evolution may be expected.

Aims. The main goal of this study is to detect and characterize, for the first time, the UCD population of compact groups of galaxies. For that, two nearby groups in different evolutionary stages, HCG 22 and HCG 90, were targeted.

Methods. We selected about 40 UCD candidates from pre-existing photometry of both groups, and obtained spectra of these candidates using the VLT FORS2 instrument in MXU mode. Archival HST/ACS imaging was used to measure their structural parameters.

Results. We detect 16 and 5 objects belonging to HCG 22 and HCG 90, respectively, covering the magnitude range $-10.0 > M_R > -11.5$ mag. Their integrated colours are consistent with old ages covering a broad range in metallicities (metallicities confirmed by the spectroscopic measurements). Photometric mass estimates put 4 objects in HCG 90 and 9 in HCG 22 in the mass range of UCDs ($> 2 \times 10^6 M_\odot$) for an assumed age of 12 Gyr. These UCDs are on average 2-3 times larger than the typical size of Galactic GCs, covering a range of $2 \lesssim r_h \lesssim 21$ pc. The UCDs in HCG 22 are more concentrated around the central galaxy than in HCG 90, at the 99% confidence level. They cover a broad range in $[\alpha/\text{Fe}]$ abundances from sub- to super-solar. The spectra of 3 UCDs (2 in HCG 22, 1 in HCG 90) show tentative evidence for intermediate age stellar populations. The clearest example is the largest and most massive UCD ($\sim 10^7 M_\odot$) in our sample, detected in HCG 22. Its properties are most consistent with a stripped dwarf galaxy nucleus. We calculate the specific frequency (S_N) of UCDs for both groups, finding that HCG 22 has about three times higher S_N than HCG 90.

Conclusions. The ensemble properties of the detected UCDs supports two co-existing formation channels: a star cluster origin (low-luminosity, compact sizes, old ages, super-solar α/Fe), and an origin as tidally stripped dwarf nuclei (more extended and younger stellar populations). Our results imply that the UCDs detected in both groups do not, in their majority, originate from relatively recent galaxy interactions. Most of the detected UCDs have likely been brought into the group together with their host galaxies.

Key words. galaxies: groups: individual: HCG 22 and HCG 90 – galaxies: dwarf – galaxies: interactions – galaxies: star clusters

1. Introduction

Within the last decade, a new class of compact stellar systems, called “ultra-compact dwarf galaxies” (UCDs), was discovered in the cores of the Fornax, Virgo, Centaurus and Hydra galaxy clusters (Hilker et al. 1999; Drinkwater et al. 2000; Mieske et al. 2004; Hasegan et al. 2005; Jones et al. 2006; Evstigneeva et al. 2007b; Hilker et al. 2007; Mieske et al. 2007, 2008; Misgeld et al. 2008). UCDs are characterized by evolved stellar populations, half-light radii of $10 \lesssim r_h \lesssim 100$ pc and masses of $2 \times 10^6 < m < 10^8 M_\odot$ (Mieske et al. 2008). They are hence of intermediate nature between globular clusters (GCs) and dwarf elliptical galaxies, covering a mass range starting at about that of ω Cen up to almost M32. The dynamical M/L ratios of UCDs are on average about twice as large as those of Galactic globular clusters at the same metallicity (e.g. Dabringhausen et al. 2008; Mieske & Kroupa 2008; Forbes et al. 2008; Kruijssen & Mieske 2009; Taylor et al. 2010). This indicates that UCDs may mark the on-set of

dark matter domination in small stellar systems (Gilmore et al. 2007; Goerdt et al. 2008), or probe a variation of the IMF (Dabringhausen et al. 2008; Mieske & Kroupa 2008).

Several formation channels of UCDs have been discussed in the literature, of which the first two are directly related to galaxy interactions: 1. UCDs have formed from the amalgamation of many young massive star clusters in the tidal arms of gas-rich galaxy mergers (Fellhauer & Kroupa 2002); 2. UCDs are remnant nuclei of dwarf galaxies which have lost their stellar halo due to interaction with the tidal field of the galaxy cluster (Bekki et al. 2003); 3. UCDs were formed together with the main body of their host galaxies’ globular cluster system, representing the very bright tail of the globular cluster luminosity function (Mieske et al. 2004; Gregg et al. 2009). 4. UCDs originate from primordial small scale overdensities, and they survived the galaxy cluster formation and evolution processes until the present time (Drinkwater et al. 2004).

Up to now, UCDs have been mainly observed in the cores of evolved clusters, like Fornax, Virgo or Centaurus. These environments – being dominated by early-type galaxies – mark the end-point of galaxy evolution with relatively large velocity dis-

Send offprint requests to: C. Da Rocha

[★] Based on observations obtained in service mode at the VLT (programme 082.B-0882)

persions and low galaxy merger rates at present. A possible very young UCD progenitor has been observed in the merger remnant NGC 7252, and UCDs have also been detected in small loose groups, like Dorado, CenA and Sombrero (Evsstigneeva et al. 2007a; Hau et al. 2009; Taylor et al. 2010).

Surprisingly, no searches for UCDs have been performed in such environments where galaxy interactions and transformation occur very often, namely in Compact Groups of Galaxies. It is therefore the proper environment to test galaxy interaction driven UCD formation scenarios. Observations and simulations are showing that great part of the galaxy evolution and “pre-processing” happens in groups (Fujita 2004; Rudick et al. 2006). Merging and subsequent infall of such groups leads to the formation of the present-day galaxy clusters. Compact groups are an environment where the evolution of galaxies occurs under the most extreme conditions, due to their high projected densities and low velocity dispersions (Hickson et al. 1992), which implies that galaxy interactions should be frequent and efficient in driving the morphological transformation of galaxies. Signs of interaction, like morphologically distorted galaxies, are frequently found in compact groups (e.g. Mendes de Oliveira & Hickson 1994), as well as star formation regions and tidal dwarf galaxy candidates (Iglesias-Páramo & Vílchez 2001; Mendes de Oliveira et al. 2001), an intragroup diffuse light (IGL) component (Da Rocha & Mendes de Oliveira 2005; Da Rocha et al. 2008) all of which shows the effects of galaxy interactions in such environments. Since the formation of UCDs is believed to be interaction driven (see above), compact groups are an ideal place to look for UCDs and test these proposed formation scenarios. Galaxies in HCGs have globular cluster systems (GCSs) typical for the host galaxy luminosity (Da Rocha et al. 2002, 2003).

In this paper we present for the first time a spectroscopic search for UCDs in the two compact groups HCG 22 and HCG 90 ($(m - M) = 32.6$ mag for both groups, corresponding to $d = 33.1$ Mpc, Blakeslee et al. 2001) using the FORS2 instrument at the VLT in MXU mode, complemented with high resolution imaging from archival Hubble Space Telescope (HST) WFPC2 and ACS data.

HCG 90, as originally catalogued by Hickson (1982), consists of four giant galaxies, the Sa NGC 7172 (HCG 90a), the E0’s NGC 7176 and 7173 (HCG 90b and c, respectively) and the irregular NGC 7174 (HCG 90d), with magnitudes in the range $M_B = -20.3$ and -19.8 (Hickson et al. 1989). Twelve smaller member galaxies, fainter than Hickson’s magnitude range, were latter identified by de Carvalho et al. (1997) and Zabludoff & Mulchaey (1998), leading to a group mean radial velocity of 2545 ± 58 km s⁻¹ and velocity dispersion of 193^{+36}_{-33} km s⁻¹ (Zabludoff & Mulchaey 1998). The group’s angular diameter is about 9’. NGC 7172 falls out of our observed field of view. The other three galaxies show optical signs of interaction (Mendes de Oliveira & Hickson 1994), an ionized gas disk at NGC 7172, a common warm gas envelope at the pair NGC 7176 and 7174 (Plana et al. 1998; Castañeda & Hilker 2004) and a diffuse X-ray halo (Mulchaey & Zabludoff 1998; White et al. 2003; Osmond & Ponman 2004). It has also a significant component of intragroup diffuse light, constituting about 35% of its stellar component of the observed part of the group (Da Rocha & Ziegler 2010 - in preparation), with colours consistent with old stellar population, showing that this group is in an advanced evolutionary stage, which is in agreement with other dynamical evolution indicators such as its crossing time

($\approx 0.02 t_{\text{Hubble}}$) and low fraction of spiral galaxies (Hickson et al. 1992).

HCG 22, as originally catalogued by Hickson (1982), consists of three giant galaxies, E2 NGC 1199 (HCG 22a) the Sa NGC 1190 (HCG 22b) and the SBcd NGC 1189 (HCG 22c), with magnitudes in the range from $M_B = -20.4$ to -18.1 (Hickson et al. 1989). An additional smaller member galaxy was latter identified by de Carvalho et al. (1997), leading to a group mean radial velocity of 2629 ± 33 km s⁻¹ and velocity dispersion of 40 ± 28 km s⁻¹ (Ribeiro et al. 1998). The group’s angular diameter is about 6’. This group is in an earlier evolutionary stage, as indicated by the low number of optical signs of galaxy interaction (Mendes de Oliveira & Hickson 1994), its larger crossing time ($\approx 0.2 t_{\text{Hubble}}$), high spiral fraction (Hickson et al. 1992) and H α content (Verdes-Montenegro et al. 2001). This group shows no signs of intragroup light, where most of the optical luminosity is concentrated on its brightest galaxy (NGC 1199). Also the the X-ray emission in the group is centered on this galaxy (Ponman et al. 1996; White et al. 2000). NGC 1199, considered to be the dominant galaxy at the group center is also the galaxy with the richest GCS among the group members.

The differences between the two groups, especially the distribution of the optical and X-ray emission (and mass, assuming light traces the mass), and the signs of recent or old interaction are an important factor in understanding the formation mechanisms of objects like the UCDs.

2. Observations and data reduction

2.1. Observations

The spectroscopic data for this study were obtained in October/November 2008 in MXU mode with the FOcal Reducer and Spectrograph FORS2 (Appenzeller et al. 1998) mounted on UT1 Antu at the VLT (programme 082.A-0882, PI: Da Rocha), using the 600B grism. FORS2 is equipped with two 2k x 4k MIT CCDs (15 μ m pixel size), and has a pixel scale of 0’25 for the commonly used SR collimator position, providing a $7 \times 7'$ field-of-view. The 600B grism is centered on 465 nm and provides a resolution of 0.75 Å per pixel. We adopted a slit-width of 1”, such that our instrumental resolution was $\approx 3\text{Å}$, corresponding to $R \approx 1500$ or about 200 km s⁻¹ (in terms of FWHM). For each mask, three exposures of 2914 seconds were taken, with a total of 8742 seconds per mask (about 2.4 hours). Figure 1 shows the $7 \times 7'$ FORS2 pre-images in the *R*-band of the two target Hickson Compact Groups 22 and 90, each corresponding to a physical scale of about 65×65 kpc at the adopted distance to HCG 22 and HCG 90 of 33.1 Mpc.

In order to measure the structural properties of our targets we have accessed HST/ACS and WFPC2 archival imaging data of the two compact groups. These images were acquired in 2006 and 2007 as part of programs GO 10554 (PI: R. Sharples) and GO 10787 (PI: J. Charlton) for HCG 90 and HCG 22, respectively. The ACS/WFC observations of HCG 90 consist of one pointing centered between the two most luminous galaxies (NGC 7173 and NGC 7176) at RA = $22^h02^m3^s94$ and DEC = $-31^{\circ}59'04''34$. Four dither line exposures with total integration time of 1375 and 3075 seconds were taken in F475W (1×340 , 3×345 seconds) and F850LP (1×639 , 774 and 2×831 seconds), respectively. The HCG 22 field was covered with four sub-pixel dithered exposures with WFPC2 totaling 1900 seconds (1×400 and 3×500 sec) in the F450W, F606W and F814W filter set. The positions and orientation of the HST observations are overlaid on the FORS2 pre-images in Figure 1 as well. Both, the ACS and

the WFPC2 imaging programs target the star cluster populations around the galaxies of the corresponding groups. The ACS imaging exposure times were designed to reach about a magnitude beyond the GC luminosity function turnover ($M_{V,TO} \simeq -7.4$ mag) while the WFPC2 observations reach about two magnitudes above ($M_V \gtrsim -9.0$ mag) at signal-to-noise of 30 and 10, respectively. This makes them ideal in depth and resolution for the purposes of the current study to measure structural and photometric properties of spectroscopically confirmed UCD candidates.

2.2. Candidate selection

For both HCGs, we used deep multi-band optical photometry covering the central $7'$ (65 kpc), in addition to the shallower R -band pre-imaging shown in Figure 1. For HCG 22, these are B and R images taken with Keck at $\simeq 0''.8$ seeing (Da Rocha et al. 2002, see their Figure 1). For HCG 90, these are FORS1 archive images of one field in B , V and R -band (programme 65.N-0547(A); Da Rocha & Ziegler 2010 - in preparation). We selected unresolved sources as UCD candidates from these deep imaging, and re-observed the same fields in the R -band during the pre-imaging for our MXU run to obtain accurate relative coordinates. We used the SExtractor star-classifier to separate unresolved from resolved sources, and furthermore performed visual inspection to cross-check the SExtractor classifications. This restriction to unresolved sources corresponds to an upper limit of projected half-light radius of about $r_h \simeq 50 - 60$ pc at the distance of HCG 22 and HCG 90, encompassing the size range of all but two of the known UCD population. In the mask creation process we assigned low priorities both to objects too red to be at redshift 0 ($(B - R)_0 > 2.0$ mag) and very blue objects ($(B - R)_0 < 0.6$ mag) to exclude foreground stars. The blue limit corresponds to a single stellar population of 1 Gyr age at metallicity $[\text{Fe}/\text{H}] = -2.0$ dex, or 0.5 Gyr age at metallicity $[\text{Fe}/\text{H}] = 0.0$ dex, according to Worthey (1994) and Bruzual & Charlot (2003), thus potential UCD candidates younger than 0.5-1 Gyr were not included in our spectroscopic sample. We further restrict to objects in the UCD magnitude regime $-14.0 < M_{R,0} < -10.0$ mag ($19.0 < R < 23.0$ mag) (Figure 2). The faint magnitude limit overlaps with the regime of massive globular clusters.

For each group we designed two MXU masks containing most of the high priority candidates (Figure 2) For each mask the planned total exposure time was 2.4 hours.

For HCG 22, both of these masks were observed in service mode, yielding spectra for 54 objects, of which seven were in common between both masks for consistency check. Of the spectra for the 47 individual sources, 10 were too faint for reliable radial velocity measurement, yielding 37 successfully observed sources of which 29 were of high priority (i.e. fulfilling the colour-magnitude selection criteria as outlined above). This compared to a total number of 38 high priority sources detected on the pre-images leads to a completeness of 76% (29/38) of the high priority candidates in HCG 22 with radial velocity measurements.

Only one mask was observed for HCG 90, containing 28 objects, of which all got reliable radial velocity measurement. 23 of those were high priority candidates. This compared to a total number of 47 high priority sources detected on the pre-images, makes our completeness for HCG 90 high priority candidates with measured radial velocities of 49% (23/47).

2.3. Data reduction: VLT Spectroscopy

The data reduction of the MXU spectra was executed with standard IRAF routines in the TWODSPEX and ONEDSPEX packages. We performed cosmic ray rejection on each of the three raw 2D spectra for each mask, using the LACOSMIC algorithm (van Dokkum 2001). We then averaged the three single, cosmic ray-cleaned exposures without applying any further rejection algorithm. Spectrum offsets perpendicular to the dispersion direction were negligible between the three single exposures. The spectra on the combined image were extracted using the APALL task in the TWODSPEX package, and wavelength calibrated using the identify and DISPCOR task in the ONEDSPEX package.

To measure the radial velocities of our targets, we performed Fourier cross-correlation with a template spectrum using the IRAF task FXCOR in the RV package. As reference template we used a synthetic spectrum of the stellar population of a typical early-type galaxy (e.g. also Mieske et al. 2002, 2004, 2008; Misgeld et al. 2008, 2009). We double-checked the radial velocity cross-correlation measurements with an alternative old stellar population template (NGC 4636, Schuberth private communications and Schuberth et al. 2009), giving consistent results. Finally, for those sources with too low cross-correlation amplitude to derive fiducial radial velocities, the cross-correlation was repeated using a 'younger' SSP template by Coelho et al. (2007) for an age of 3 Gyrs and $[\text{Fe}/\text{H}] = -0.5$ dex. This led to the detection of one additional compact group member in HCG 22, see Section 3.

In Figure 3 we show example spectra and cross-correlation results for three objects classified as group members according to their radial velocity.

2.4. Data reduction: HST Imaging

We used two data products provided by the HST reduction pipeline - the *flt* and the *drz* images. To avoid problems arising from the image resampling due to insufficient sub-pixel dithers during the *drizzle* algorithm (Fruchter & Hook 2002) in producing the final *drz* stack images, we chose to work directly on the *flt* images for the actual measurements. The *drz* images were used for the final photometric calibrations. The *flt* images are dark, bias and flat-field corrected, and have not been resampled, therefore providing the most natural observation of the astronomical scene. However, the ACS *flt* images are still in the original WFC coordinate system which suffers from strong geometric distortions.

In order to perform the most accurate structural and point-spread function-fitting (PSF) photometry measurements of faint, barely resolved objects one has to properly take into account the varying pixel area across the ACS/WFC detectors. Anderson & King (2006) provide an empirically created library of fiducial PSFs which we used with the algorithms described in detail in Anderson & King (2000, 2006) and Anderson et al. (2008) to perform the PSF-fitting photometry¹. PSF-fitting was performed on every single F475W and F850LP exposure using the spatially varying array of empirical PSFs, plus a "perturbation PSF" tailored to each exposure to compensate for the temporal effects of focal variations. At this stage, the catalogs contain many spurious detections (hot pixels, cosmic rays, and spurious detections along diffraction spikes). Those were eliminated by

¹ The `img2xym_WFC.09x10` code was slightly modified to output the value of the local background which is important for determining the CTE corrections.

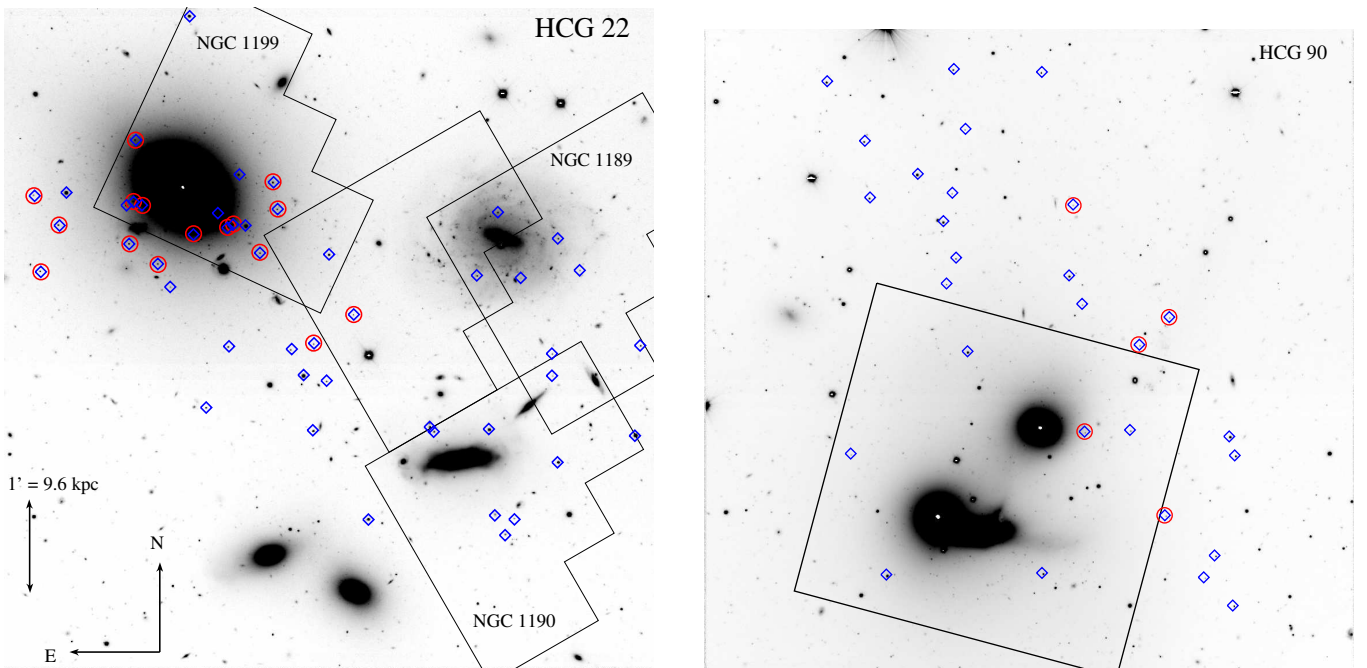


Fig. 1. FORS2 *R*-band pre-images of HCG 22 (left) and HCG 90 (right), of dimension $7 \times 7'$, corresponding to about 65×65 kpc at the distance of the groups. Blue diamonds show the spectroscopic targets and those marked with red circles are confirmed compact members of the HCGs (most in the mass range of UCDs), i.e. those with radial velocities within the group range (cf. Figure 4). Note the difference in their spatial distribution: UCD candidates in HCG 22 are clustered around the central galaxy, while the few UCDs in HCG 90 have more dispersed distribution. Overlaid are also the HST pointings used in our analysis (WFPC2 for HCG 22 and ACS/WFC for HCG 90). Labels in HCG 22 indicate the name of the target at which the WF3 chip was centered. Physical scale and orientation are indicated in the lower left corner and are the same for both fields. A colour version of this figure, showing a high-resolution HST zoom at the dusty disk in the central 5 kpc of NGC 1199 and gas dominated spiral in HCG 90, is available as an online material.

matching the coordinates of each exposure within a tolerance of 0.5 pixels. The final photometry list contains four measurements for each source per filter. The final instrumental magnitude is the goodness of fit (“qfit”) weighted average of the four measurements.

To correct for the charge transfer efficiency (CTE), which is a function of the date of observation, object brightness, background and position, we used the latest correction equation provided by Chiaberge et al. (2009). The photometry was put into the ACS/WFC Vega-mag system following Bedin et al. (2005), i.e. by comparing the CTE corrected instrumental magnitudes with the magnitudes of the same stars measured within $0''.5$ aperture radius and correction from $0''.5$ to “infinity” using the values from Table 1 in Bedin et al. (2005). We adopted the zero points from the latest and improved photometric calibration of the ACS listed on the STScI website², which supersede the previous by Sirianni et al. (2005). We used the ACS/WFC zero points at -77°C since the ACS observations were acquired in May 2006, i.e. before July 2006 when the temperature of the WFC detector was lowered to -88°C following the recovery of the ACS.

The pipeline reduced F450W, F606W and F814W WFPC2 images retrieved from the HST archive are bias, flat-field and bad pixel corrected images for each WFPC2 chip. The sub-pixel dithered imaging allowed us to eliminate cosmic-rays, hot pixels and improve the spatial resolution. For image registration we used the IRAF task WREGISTER, with flux conserving driz-

zle resampling factor of 0.8, to register the individual exposures for each CCD chip and filter combination using the solutions recorded in the image headers. This proved to give an extremely satisfactory final stack image, median combined from the four exposures with the IRAF task IMCOMBINE. We cross checked the profiles of the few stars between the original exposures and the final median combined image for each filter and the difference in FWHM was up to ± 0.02 pixels. To perform a PSF photometry on the WFPC2 images, we created a grid of 100×100 PSFs with the TinyTim³ software package (Krist 1995) for each CCD chip and filter. This library was used to create a spatially variable PSF model and perform PSF-fitting photometry with the ALLSTAR task in IRAF. Isolated stars were used to derive aperture correction to $1''.0$ aperture diameter which is the aperture used by Dolphin (2009) to derive the most up to date CTE corrections and photometric zero points for each of the WFPC2 chips.

Finally, the ACS and WFPC2 photometry, calibrated to the Vega-magnitude, was corrected for foreground extinction estimated from the Schlegel et al. (1998) dust maps toward the direction of both groups. The estimated Galactic extinction is $E(B - V) = 0.026$ and 0.055 mag for HCG 90 and 22, respectively. We used the Cardelli et al. (1989) relations and $R_V = 3.1$ to calculate the absorption at the effective wavelengths for the

² Zero points and details on the new calibrations can be found on <http://www.stsci.edu/hst/acs/analysis/zeropoints>

³ TinyTim properly takes into account the significant variation of the PSF as a function of wavelength (filter) caused by the expanding of diffraction structures with increasing wavelength, position-dependent changes of the shape of the PSF, aberrations, focus offsets between cameras (WFs and PC1 for WFPC2) and wavelength dependent charge diffusion. See also <http://www.stsci.edu/software/tinytim/>

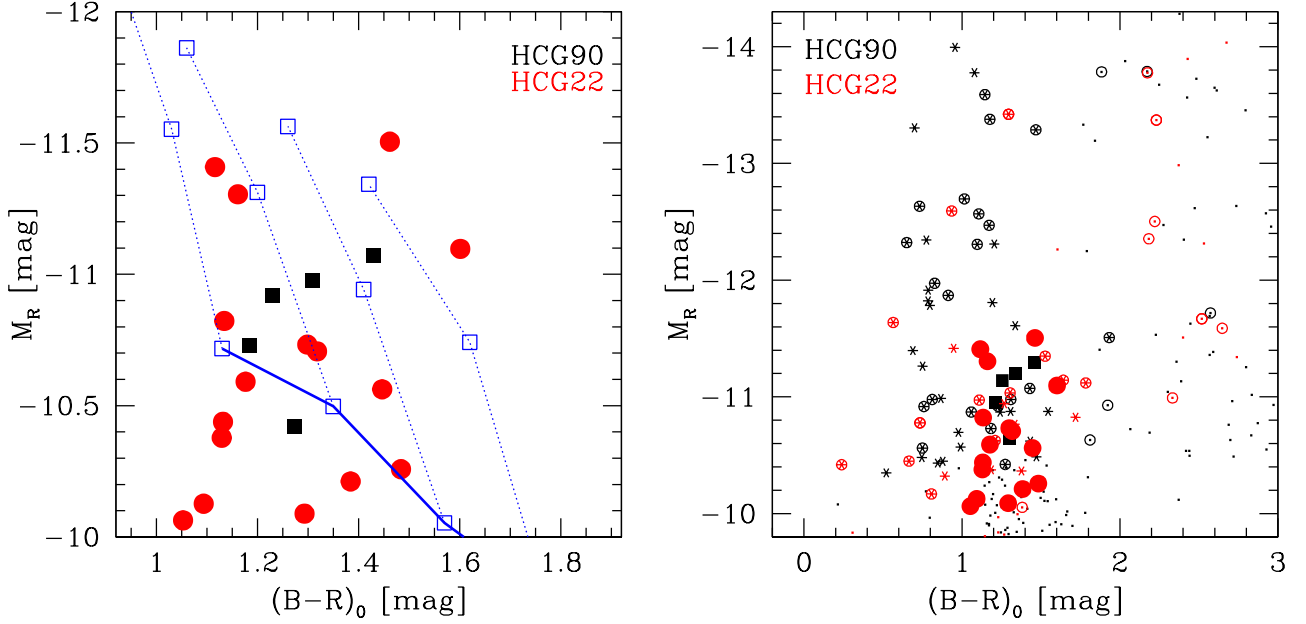


Fig. 2. Colour-magnitude diagrams of HCG compact members (left panel) and all preselected targets (right panel). **Left panel:** $(B - R)_0$ is plotted vs. M_R for spectroscopically confirmed members in the two groups. The dotted lines are model predictions for simple stellar populations from Bruzual & Charlot (2003) for a range of metallicities and ages, and a stellar mass of $2 \times 10^6 M_\odot$, which marks the limit between normal GCs and UCDS (e.g. Mieske et al. 2008). From left to right the lines correspond to metallicities $[Z/H] = -1.6, -0.6, 0.1,$ and 0.4 dex. The open squares indicate ages of 2, 5, and 12 Gyrs, from top to bottom. The solid (blue) line indicates the 12 Gyr isochrone for a stellar mass of $2 \times 10^6 M_\odot$. **Right panel:** Analogous to the left panel, but for a wider colour-magnitude range to show the confirmed group members and the preselected targets of our survey. Filled red circles and black squares indicate the confirmed group members, the same as in the left panel. Open circles indicate all other objects that were included in the MXU masks. Sources marked by asterisks are those which were high priority candidates, according to their colour-magnitude values and morphology. Small dots indicate target sources of lower priority (colours fall outside the selection color range, or of more resolved morphology).

ACS/WFC and WFPC2 filters. Thus the following dereddening values were applied for the HCG 90 ACS images: $A_{F475W} = 0.104$, $A_{F850LP} = 0.039$ mag and for the HCG 22 WFPC2 images: $A_{F450W} = 0.237$, $A_{F606W} = 0.170$ and $A_{F814W} = 0.112$ mag. The result is shown in the colour-magnitude and colour-colour diagrams (Figures 5 and 6) and discussed in Section 3.1.

2.4.1. Measuring structural parameters of UCD candidates

Measuring structural parameters of UCD candidates in HCG 22 and HCG 90 is feasible thanks to the supreme resolution of the ACS and WFPC2 cameras of $0''.05$ and $0''.1$ pixel $^{-1}$, corresponding to ~ 8 and 16 parsecs at a distance of 33.1 Mpc, respectively. Therefore, and due to the very well characterized PSF over the ACS/WFPC2's field-of-view, extended objects with half-light radius of only a few parsec will be measurable, allowing to resolve objects down to typical GC sizes. To derive the r_h of the UCD candidates in our sample from the ACS images, we generated a ten times subsampled PSF from the Anderson & King (2006) ACS/WFC ePSF library. Each PSF is tailored to the position on the chip for every object measured. This PSF was used with ISHAPE of the BAOLAB software package⁴ (Larsen 1999) which models the object profile with an analytical function convolved with a (model) PSF. We modeled all objects with King profiles with concentrations of tidal-to-core

radius of $r_t/r_c = 5, 15, 30$ and 100 and adopted the structural parameter measurements from the best χ^2 fit model. The output is the FWHM along the object semi-major axis. It is converted to R_{eff} using the coefficients relating those two values, as prescribed in the BAOLAB manual. This R_{eff} needs to be corrected for object ellipticity and brought to the geometrically mean value (“effective” r_h) by multiplying by the square root of the major/minor axis ratio (details see eq. 1 in Georgiev et al. 2008).

Measurements of the structural parameters of UCD candidates on the WFPC2 images were performed in an analogous way as for the ACS, but PSFs at the objects’ position were generated with the TinyTim for the F606W filter. Generating ten times subsampled PSFs with TinyTim does not include a convolution with charge diffusion kernel (CDK), which additionally smears the stellar PSF. The CDK available within TinyTim is applicable in the 500 - 600 nm range (F555W filter), therefore, we restricted our measurements only to the F606W filter and did not perform measurements for the rest of the filters.

We finally note that reliable r_h measurements with ISHAPE are performed for objects with $S/N > 20$ (Larsen 1999). The UCD candidates in the HCG 22 have signal-to-noise in the range $20 < S/N < 80$ and the UCD candidate in HCG 90 has $S/N = 86$.

3. Results

In Figure 4 we show a histogram of the measured radial velocities (corrected to heliocentric velocity). We detect five mem-

⁴ We used the most recent release of BAOLAB found on <http://www.astro.uu.nl/~larsen/baolab/>

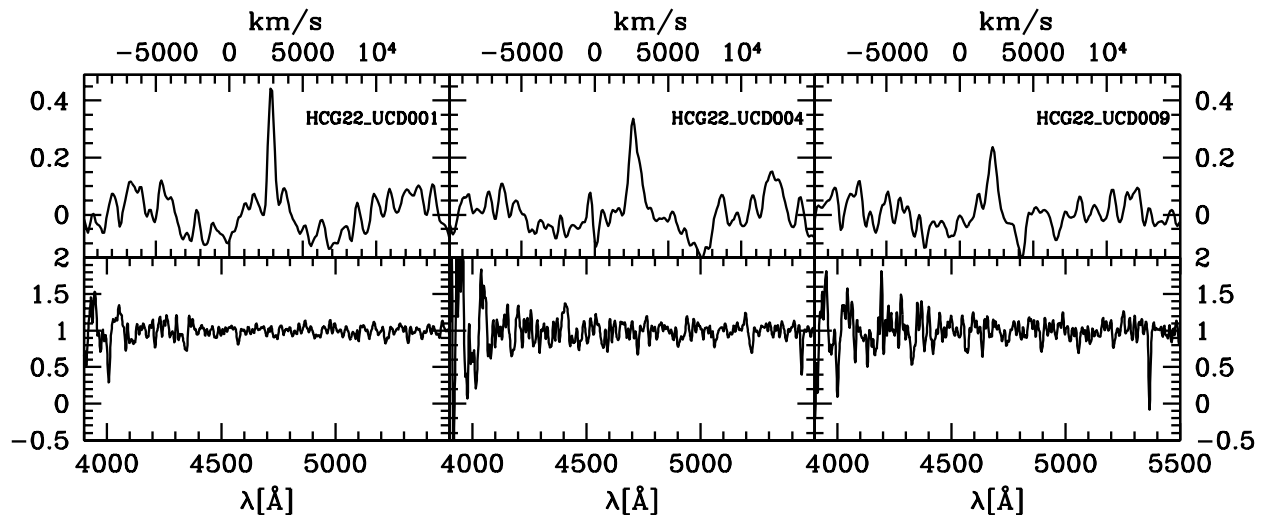


Fig. 3. Spectra (bottom panels) and cross-correlation results for radial velocity measurement (top panels) for three example HCG 22 compact objects covering our range of cross-correlation confidence level (from left to right), see also Table 1.

bers of HCG 90 and 16 members of HCG 22. Four other sources were found to be background galaxies at significantly higher redshift than the HCGs. All other targets turned out to be foreground stars. We note that one of the 16 members in HCG 22 (HCG22_UCD011) was detected only via cross-correlation with the intermediate age (3 Gyr) SSP template (Coelho et al. 2007), instead of the reference old stellar population template. Besides for excluding very young objects, our selection criteria were satisfactorily efficient, in the UCD richer group (HCG 22), more than 50% of the high priority targets we indeed objects belonging to the group.

The properties of all compact objects are summarized in Tables 1 to 4. They span absolute magnitude ranges of $-10.4 > M_R > -11.1$ mag for HCG 90 and $-10.0 > M_R > -11.5$ mag for HCG 22. Their positions within the groups are shown with large open (red) squares on the pre-images in Figure 1. The HCG 22 UCD candidates are clearly clustered around the group dominant galaxy NGC 1199, while the distribution in HCG 90 is more uniform over the group area.

Their R vs. $(B-R)_0$ colour-magnitude distribution are shown in Figure 2. In the left panel of Figure 2 are shown model predictions from Bruzual & Charlot (2003) in the colour-magnitude range of objects at the approximate mass limit of $2 \times 10^6 M_\odot$ between normal GCs and UCDs, for a range of metallicities and ages. Assuming a 12 Gyr stellar population, 9 of the 16 objects in HCG 22 are in the UCD mass range range, with $M_R \lesssim -10.4$ mag. For HCG 90, four of the five objects are in the UCD mass range range. The colour range $1.1 < (B-R)_0 < 1.65$ mag of the HCG compact members is consistent with them being old and covering a range of metallicities $-1.7 \lesssim [\text{Fe}/\text{H}] \lesssim 0.2$ dex. We note, however, that moderately metal-rich and young objects of a few Gyr would also still fall in the observed colour window.

In the colour-magnitude diagrams (CMDs) in Figure 2 we also indicate the data of all candidate compact objects, and all objects that were observed with the MXU masks. The group member detections, indicated as filled circles, concentrate towards the faint end of our survey. We have not found very massive UCD candidates with $M_R \approx -14.0$ ($\approx 10^8 M_\odot$) as seen in the

Fornax and Virgo galaxy clusters, nor presumably young UCDs among the blue candidates in the covered colour range.

In Section 3.1, we present the sizes and colours derived for a subsample of UCD candidates from HST imaging. In Section 3.2 we analyze the kinematics and spatial distribution of the UCD candidates, and in Section 3.3 we discuss their stellar populations.

3.1. Sizes and colours from the HST imaging data

Important constraints on the nature of the detected UCD candidates can be obtained from the high resolution HST imaging. In Figures 5 and 6 we show the colour and magnitude distributions of all measured objects in the ACS/WFC and WFC2 fields of view. In Figure 7 are shown the half-light radius measurement as a function of object luminosity and colour for all objects with spectroscopy in our sample. Here we focus our discussion on the properties of the UCD candidates preselected from the spectroscopic sample.

All UCD candidates are consistent with the expectations from simple stellar population (SSP) evolutionary models (GALEV⁵ by Anders & Fritze-v. Alvensleben 2003; Kotulla et al. 2009) for old ages and the entire range in metallicities. The comparison in Figure 5 between the only UCD candidate (HCG90_UCD005) within the ACS field of HCG 90 and the SSP model with a mass of $5 \times 10^6 M_\odot$, shows that the UCD candidate can be as massive as $\sim 10^7 M_\odot$. This is consistent with the estimate obtained from the ground-based photometry in Figure 2, indicating that HCG90_UCD005 falls in the transition mass regime between UCDs and GCs. Its light profile is best fit by a King model with concentration $c = r_t/r_c = 100$ and a half-light radius of $r_h = 3.13$ pc. The r_h is typical for GCs, and thus HCG90_UCD005 morphologically classifies rather as a star cluster than as a UCD. Unfortunately, it has too low S/N spectrum for quantitative abundance analysis. This object is indicated by a solid pentagon in Figure 7. The other brighter sources with

⁵ <http://www.galev.org/>

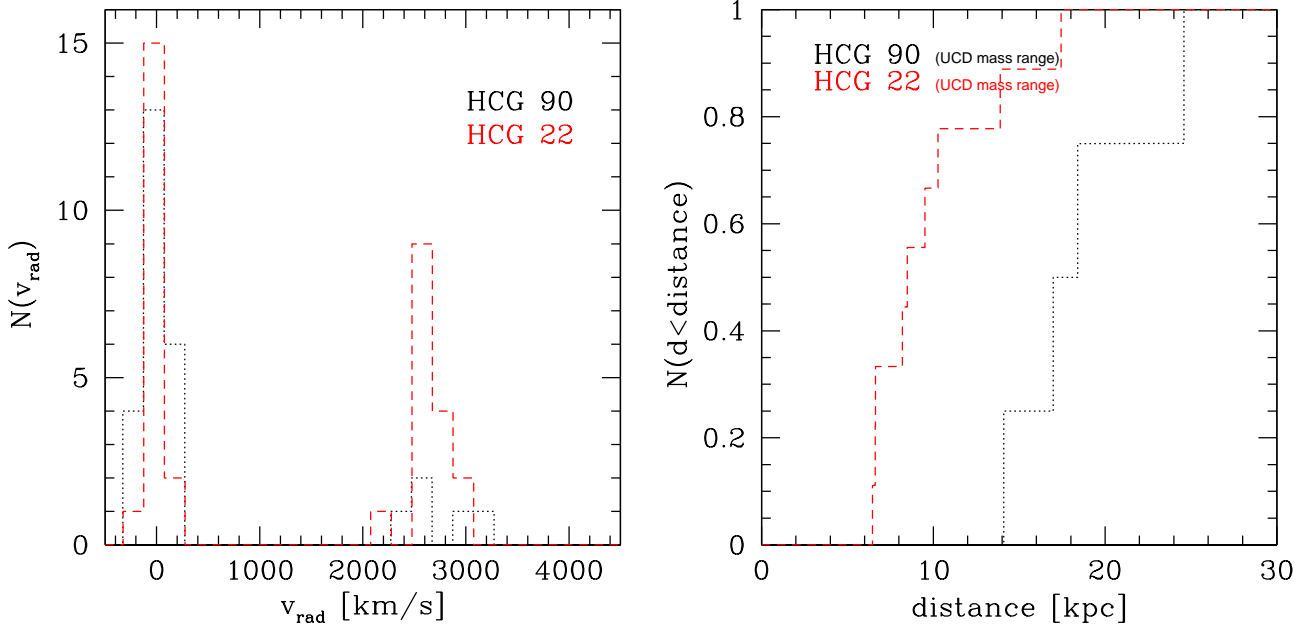


Fig. 4. Left panel: Radial velocity histogram (corrected to heliocentric velocity) of spectroscopic targets in HCG 22 (red) and HCG 90 (black). The group members at around 2700 km s^{-1} are well separated from foreground stars and background galaxies with extreme velocities (not shown for clarity). **Right panel:** Cumulative radial distance distribution of the HCG compact members relative to the central galaxies (NGC 1199 and NGC 7173 for HCG 22 and 90, respectively). The samples in this panel are restricted to the UCD mass range. The KS-test probability of both distributions having the same parent distribution is 0.9%.

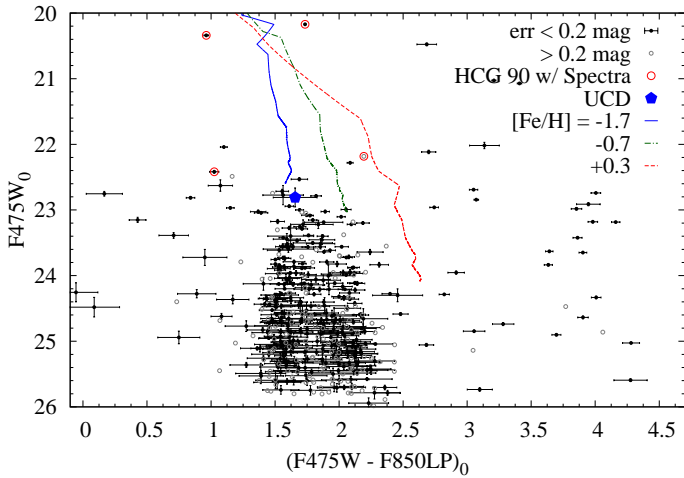


Fig. 5. Colour-magnitude diagram of all sources in the HCG 90 WFC/ACS field of view. The UCD candidate is indicated with a solid pentagon while large open circles indicate all sources for which spectroscopy is available. For comparison, GALEV SSP model isometallicity tracks are shown with lines for three fiducial metallicities (Anders & Fritze-v. Alvensleben 2003; Kotulla et al. 2009), as indicated in the figure’s legend. The models luminosities are for a cluster of $5 \times 10^6 M_{\odot}$.

spectra (circles in Figure 5) are foreground stars which is further confirmed by their $r_h \simeq 0 \text{ pc}$, i.e. their PSF is indistinguishable from a stellar PSF (cf. Figure 7).

Figure 6 shows the colour-magnitude and colour-colour diagrams of sources in the four HST/WFPC2 pointings covering most of HCG 22. We have labeled these fields with the name of the target at which the WF3 chip was centered. These are the

galaxies in this group (the brightest NGC 1199, NGC 1189 and NGC 1190) and one pointing in between them. Ten of the 16 HCG 22 UCD candidates are within the WFPC2 fields. Nine of those are within the NGC 1199 pointing, the other in the mid-group pointing. All of them are brighter than the $5 \times 10^6 M_{\odot}$ SSP models (see also Figure 2), thus falling into the mass range of UCDS. The most luminous UCD candidate has an inferred mass of $\simeq 10^7 M_{\odot}$. We note that the dynamical M/L ratios of UCDS in other environments have been found to be 50-100% above predictions from SSP models (e.g. Mieske et al. 2008; Dabringhausen et al. 2008), and are on average around $M/L = 4 - 5$. Adopting this average M/L ratio instead of $M/L \sim 3$ characteristic for the SSP models in Figure 5 and also typical for the most metal-rich Galactic GCs, the implied mass range of our UCD candidates would extend to about 50% larger values up to $\sim 2 \times 10^7 M_{\odot}$.

The candidates have a broad range of half-light radii $2 < r_h < 21 \text{ pc}$ with a mean of $r_h = 7.4 \pm 1.5 \text{ pc}$. That is, they are on average 2-3 times larger than typical GCs and up to four times more massive than ωCen , hence they can be classified as UCDS. It is interesting to note the apparent concentration of blue objects on the NGC 1189 and “Mid Group” colour-colour diagrams (bottom row the left and right most panels). NGC 1189, covered by the “Mid Group” WFPC2 field, is a face-on, active star-forming SBcd which is the group brightest galaxy in UV wavelengths (Tzanavaris et al. 2010). Therefore, young objects, like unresolved star-forming regions, young star clusters are expected to be present in our color-magnitude diagrams. NGC 1190 and 1199 are considered as passive galaxies and the absence of blue (young) sources is expected.

The photometric and structural properties of the observed UCD candidates are summarized in Tables 3 and 4.

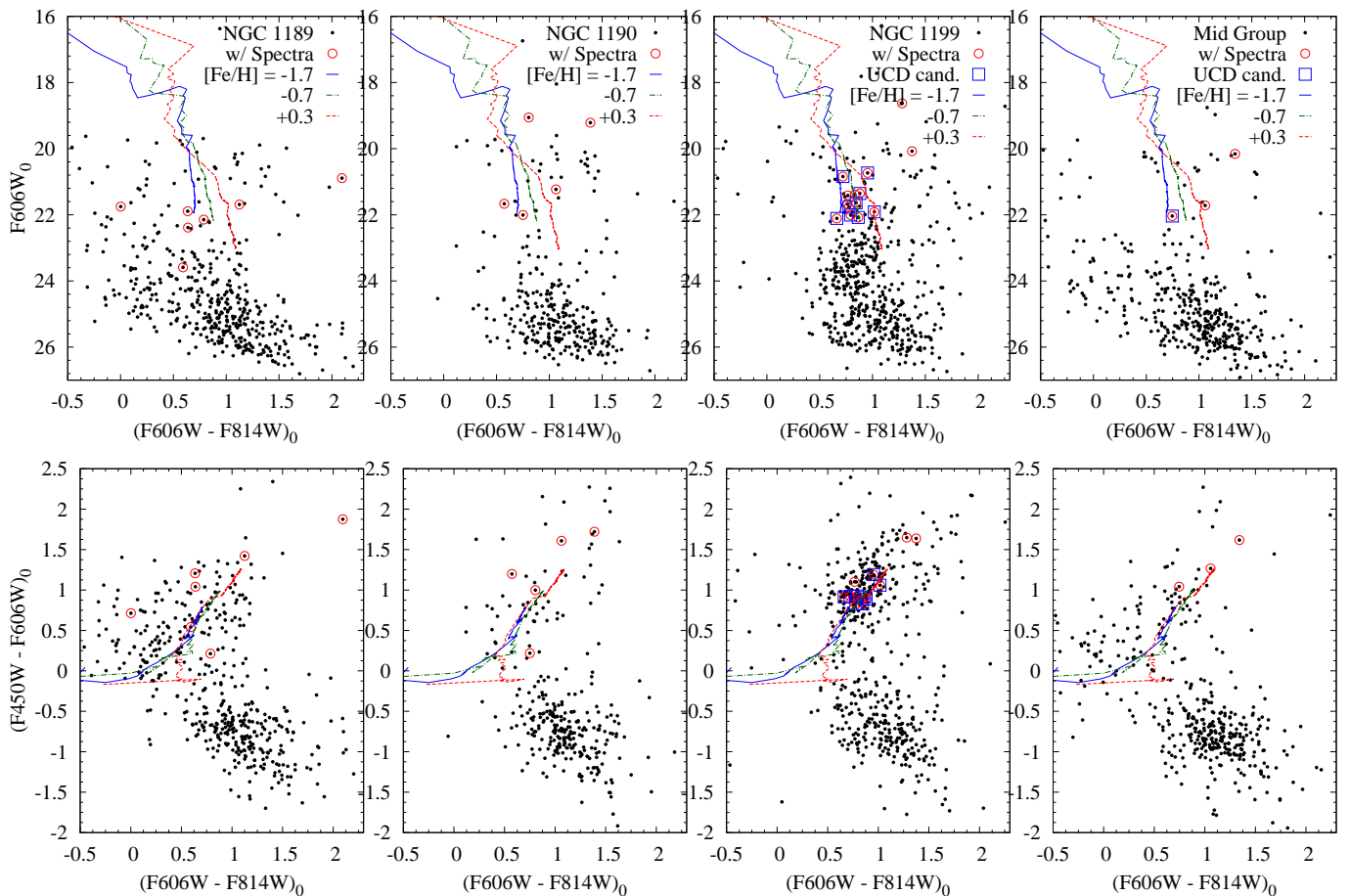


Fig. 6. Top row: Colour-magnitude diagrams for all objects (dots) in HCG 22 for each of the four WFPC2 pointings. The legend for each CMD indicates the galaxy/region at which the WF3 chip was centered. **Bottom row:** Colour-colour diagrams of all sources (dots) with photometry for the same fields. In all panels the open circles indicate the objects with spectroscopy while the open squares are the UCD candidates. The description of the SSP isometallicity tracks is the same as in Figure 5.

3.2. Kinematics and spatial distribution

For HCG 22, the mean velocity and dispersion of the 16 HCG compact members are $v_{\text{mean,HCG22}} = 2664 \pm 47 \text{ km s}^{-1}$ and $\sigma_{\text{HCG22}} = 171^{+71}_{-40} \text{ km s}^{-1}$, where σ was corrected for internal errors using Danese et al. (1980) and the stated errors correspond to a 90% confidence interval. For HCG 90, the values are $v_{\text{mean,HCG90}} = 2608 \pm 109 \text{ km s}^{-1}$ and $\sigma_{\text{HCG90}} = 206^{+405}_{-80} \text{ km s}^{-1}$. The mean radial velocities are in good agreement with the group values, $v_{\text{mean,HCG22}} = 2629 \pm 33 \text{ km s}^{-1}$ and $v_{\text{mean,HCG90}} = 2545 \pm 58 \text{ km s}^{-1}$ (Ribeiro et al. 1998; Zabludoff & Mulchaey 1998). The velocity dispersions for the UCD candidates in HCG 90 agrees well with the group value ($193^{+36}_{-33} \text{ km s}^{-1}$ Zabludoff & Mulchaey 1998) showing no kinematical decoupling from the overall galaxy population, while the dispersions for candidates in HCG 22 is considerably higher than the group value ($40 \pm 28 \text{ km s}^{-1}$ Ribeiro et al. 1998), being more consistent with the internal velocity dispersion of NGC 1199 ($207 \pm 21 \text{ km s}^{-1}$ Prugniel & Simien 1996).

In HCG 22, we detect about twice as many UCD candidates as in HCG 90 (9 vs. 4), but taking into account the lower completeness for HCG 90 (76% for HCG 22 and 49% for HCG 90), this difference is not significant. Figure 1 shows that the compact objects in HCG 22 appear to be more strongly clustered around

the group’s central galaxy than is the case for HCG 90, a possible evidence of their origin being associated to processes related to its central galaxy (NGC 1199). In Figure 4 right panel, we compare the cumulative radial distance distribution of UCD candidates in HCG 22 and HCG 90 with respect to the central galaxy (NGC 1199 and NGC 7173 for HCG 22 and 90, respectively). Applying a Kolmogorov-Smirnov-test (KS test), the probability that the HCG 22 and HCG 90 radial distance distributions are drawn from the same parent population is only 0.9%. This result confirms the visual impression of a stronger clustering in HCG 22. We note that our magnitude cut for excluding objects in the GC magnitude range excludes the HCG 90 source with closest projected distance to the central galaxy. Including this object into the KS test still yields a probability of only 4%.

3.3. Stellar populations

We have measured Lick line indices for all the compact group members detected, using the passband definitions from Trager et al. (1998), having smoothed the spectra to match the 9 \AA Lick system resolution. From measurements of six Lick standard stars taken in the same setting and smoothed in the same way, we could not detect any significant deviation between tabulated Lick line index values and our measurements down to a

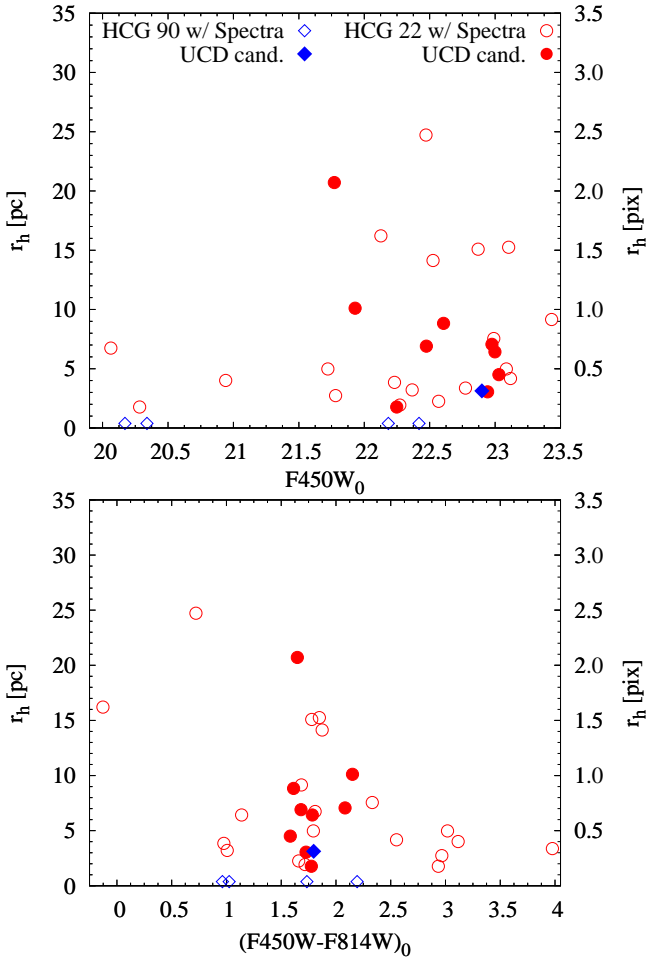


Fig. 7. Distribution of the half-light radius in parsecs (left axis) and pixels of 0.1 (right axis) versus the luminosity (top) and colour (bottom) of objects with spectroscopy in HCG 90 and 22. Blue pentagons show objects with spectra in HCG 90 and red circles in HCG 22. Solid symbols mark the UCD candidates in both groups. Unresolved objects in this figure will have sizes close to $r_h = 0$. Pixel to parsec conversion in both panels corresponds to the WFPC2 pixel scale (0.1 pix^{-1}). Thus, HCG 90 objects will have twice the pixel value on the y-axis, because of the higher resolution of the ACS/WFC (0.05 pix^{-1}). For comparison purpose, ACS (F475W-F850LP) colours were transformed to the WFPC2 (F450W-F814W) using GALEV (Anders & Fritze-v. Alvensleben 2003; Kotulla et al. 2009) for the metallicity range of our objects.

level of $\sim 0.1 \text{ \AA}$. Given the much larger measurement errors of our science targets (see below) we therefore do not apply any correction.

A commonly used metallicity sensitive index is $\langle Fe \rangle = 0.5 \times (\text{Fe}5270 + \text{Fe}5335)$. In the following, we only show and discuss measurements for which the statistical uncertainty of the $\langle Fe \rangle$ index is less than 0.5 dex, as determined from the photon counts in the object and sky spectra. Tables 1 and 2 show the line index estimates for the five sources in HCG 22 and three sources in HCG 90 with errors below 0.5 dex.

We also indicate an estimate of the corresponding $[\text{Fe}/\text{H}]$. For this we use for $[\text{Fe}/\text{H}] < -0.4$ dex the empirical calibration between $[\text{Fe}/\text{H}]$ and $[\text{Mg}/\text{Fe}]$ derived by Puzia et al. (2002) from galactic GCs. For $[\text{Fe}/\text{H}] > -0.4$ dex we adopt an extrapolation

of the form $[\text{Fe}/\text{H}]_* = a + b \times \log(\text{Mg}/\text{Fe})$ that matches the calibration for $[\text{Fe}/\text{H}] < -0.4$ dex (see also Mieske et al. 2007).

In Figure 8 we show diagnostic plots for age and alpha abundances, using model predictions from Thomas et al. (2003). From the left panel it can be seen that the two most metal-rich UCD candidates in either groups, appear most consistent with super-solar alpha abundances of 0.3 to 0.5 dex. Furthermore, in the age diagnostic plot in the right panel, it is clear that all three UCD candidates in HCG 90 are most consistent with old ages of around a Hubble time. For HCG 22, object HCG22_UCD002 is inconsistent with an old age of 12 Gyr, indicating the presence of an intermediate age stellar population. The other sources have too large error bars to make strong statements.

To further investigate the possibility of intermediate age UCDs, we show in Figure 9 the ratio of the cross-correlation amplitude of our reference old stellar template (see also Mieske et al. 2002, 2004, 2008; Misgeld et al. 2008, 2009), and the intermediate age stellar template of 3 Gyrs and $[\text{Fe}/\text{H}] = -0.5$ dex from Coelho et al. (2007). We define this ratio as $\psi_{12/3} = \log(\text{XcorAmp}(12\text{Gyr})/\text{XcorAmp}(3\text{Gyr}))$. Sources which are better fit by the old stellar template lie above the (dashed) identity line, while sources fit better by the intermediate age template lie below the line. There are two UCD candidates, HCG22_UCD011 and HCG90_UCD004, which are distinctively better fit by the intermediate age stellar template. Those two sources are good candidates for intermediate age UCDs. Unfortunately, the spectra were not of sufficiently high S/N to investigate this possibility via line index measurements. It is noteworthy that HCG22_UCD002 is, after HCG22_UCD011, the source with the second best intermediate age fit in HCG 22. This supports the indications from line index measurements that this object also contains intermediate age stellar populations. On average, UCDs in HCG 90 are fit slightly better by the intermediate age stellar template than UCDs in HCG22 (cf. Figure 9).

4. Discussion and Conclusion

4.1. Summary of the results

Before proceeding with the discussion, in the following we present a summary of the main results.

(1) We detected 16 and 5 objects belonging to HCG 22 and HCG 90, respectively. They cover the magnitude range $-10.0 > M_R > -11.5$ mag for HCG 22 and $-10.4 > M_R > -11.1$ mag for HCG 90. Their colours are consistent with old stellar populations covering a broad range of metallicities. Metallicity estimates from line index measurements for a sub-sample of objects with sufficiently high S/N cover a range of $-1.0 \lesssim [\text{Fe}/\text{H}] \lesssim 0.3$ dex.

(2) Photometric mass estimates using Bruzual & Charlot (2003) put four objects in HCG 90 and nine objects in HCG 22 in the mass range of UCDs ($> 2 \times 10^6 M_\odot$) for an assumed age of 12 Gyr.

(3) The detected objects are on average 2-3 times larger than the average size of Galactic GCs, covering a range of $2 \lesssim r_h \lesssim 21$ pc.

(4) The mean velocities of the UCDs agree with the galaxy group values. The velocity dispersion of HCG 90 UCDs is similar to that of the galaxies in the group, while the velocity dispersion of HCG 22 UCDs is more consistent with the internal dispersion of NGC 1199.

(5) The UCDs in HCG 22 are more concentrated around the central galaxy than in HCG 90, at the 99% confidence level.

(6) We find two UCDs in HCG 22 and one in HCG 90 with evidence for an intermediate age stellar population (3-5 Gyrs),

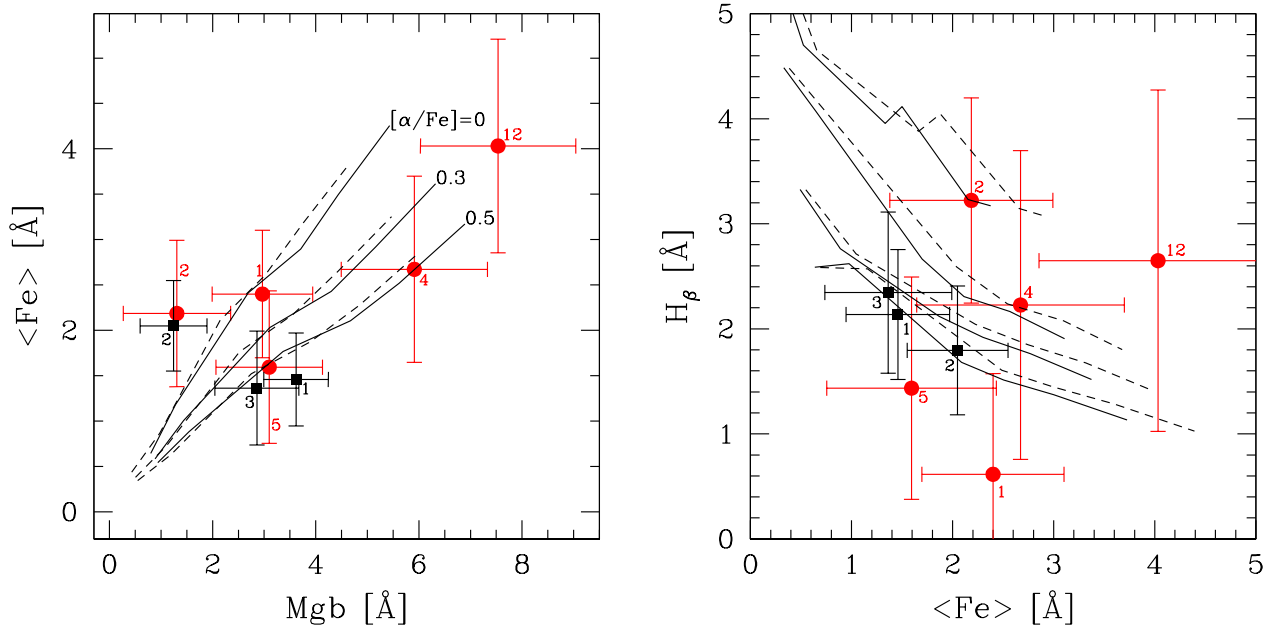


Fig. 8. Lick line index diagnostic plots for a sub-sample of the compact group members with high enough S/N (error in $\langle Fe \rangle$ index below 0.5 dex). **Left panel:** Diagnostic plot for alpha abundances, plotting $\langle Fe \rangle$ vs. Mgb index. We show lines of identical alpha abundances for both age of 12 Gyr (solid line) and 4 Gyr (dashed line), using the model predictions of Thomas et al. (2003). The two most metal-rich members of either group appear to have super-solar alpha abundances. **Right panel:** Diagnostic plot for age estimation, plotting H_β vs $\langle Fe \rangle$ index for four different ages 12, 7, 3, and 1 Gyr from bottom to top (solar α -abundance). The three UCDs in HCG 90 appear consistent with very old ages, as do the two HCG 22 UCDs HCG22_UCD001 and HCG22_UCD005 (see Tables 1 and 2). Numbers on the symbols are the ID of each object, where the prefixes were omitted for clarity.

based on spectral cross-correlation with old and intermediate age templates and Lick line index measurements. The clearest example for this is the largest and most massive UCD ($\sim 10^7 M_\odot$) in our sample, detected in HCG 22.

4.2. The newly detected UCDs in the group context

The two investigated Hickson Compact Groups present different evolutionary stages. While HCG 22 has no evidence of intragroup light, HCG 90 has about a third of its total light in the IGL component (Da Rocha & Ziegler 2010 - in preparation). Also the X-ray properties of the groups are different. Ponman et al. (1996) established an upper limit for the ROSAT detection of HCG 22 and White et al. (2000) detected NGC 1199, presumably the group center, around which the UCDs are concentrated, as a point source on a new analysis of ROSAT data. In HCG 90 a diffuse X-ray component was detected, which shows strong emission on the interacting pair NGC 7174/7176 and is in good agreement with the space distribution of the IGL component, in addition to individual emission from the member galaxies (Ponman et al. 1996; Mulchaey & Zabludoff 1998; White et al. 2003; Osmond & Ponman 2004; Treister et al. 2005).

The spatial distribution of UCDs in each group is not discrepant with the respective distribution of the overall light (and stellar mass) in each group. HCG 22 is a very concentrated structure with three galaxies and NGC 1199 represents about 75% of the group's luminosity. Hence the concentration of UCDs around NGC 1199 is not too surprising, since even a component associated to the group's potential would mainly be distributed around this galaxy, as is its GCS (Da Rocha et al. 2002). In contrast, HCG 90 has a much more uniform luminosity distribu-

tion, where the difference between the brightest and the faintest galaxy is less than 10% of the total group luminosity and the brightest component is the IGL, in which the three studied galaxies and the UCDs are embedded. The more uniform mass/light distribution is reflected by the spatial distribution of the UCDs found in this group.

How does the specific frequency of UCDs (number of UCDs normalized by the total light of the group in the B -band) in either group compare? This quantity can be useful to compare the richness and/or formation efficiency of UCDs in different galaxy groups and clusters. We define the UCD specific frequency normalized to $M_B = -20$ mag, hence $S_{N,UCD} = N_{UCD} \times 10^{0.4 \times (M_B + 20)}$. This normalization results in UCD specific frequencies of comparable numerical values to GC specific frequencies, yielding for example $S_{N,UCD} \approx 1$ for the case of a single UCD in an L_* galaxy. For our purposes we need to restrict the group luminosity estimate in HCG 90 to the 3 of the 4 group galaxies covered by our survey, but include the diffuse intragroup light fraction of $\sim 35\%$ which was not taken into account by Hickson et al. (1989). Assuming the same distance modulus ($m - M$) = 32.6 mag for both groups, we find a total B -band luminosity of $M_B = -21.5$ mag for HCG 90 within our survey area, and $M_B = -20.7$ mag for HCG 22 (Hickson et al. 1989). Taking into account the number of 4 and 9 UCDs found in either group and the corresponding survey incompleteness, we get $S_{N,UCD,HCG90} = 2.0 \pm 1.0$ and $S_{N,UCD,HCG22} = 6.3 \pm 2.1$. This difference of about a factor of three indicates that the formation process of UCDs has been more efficient in HCG 22 than in HCG 90.

We can extrapolate the GC luminosity function (GCLF) estimated for NGC 1199 in HCG 22 (Da Rocha et al. 2002) to the

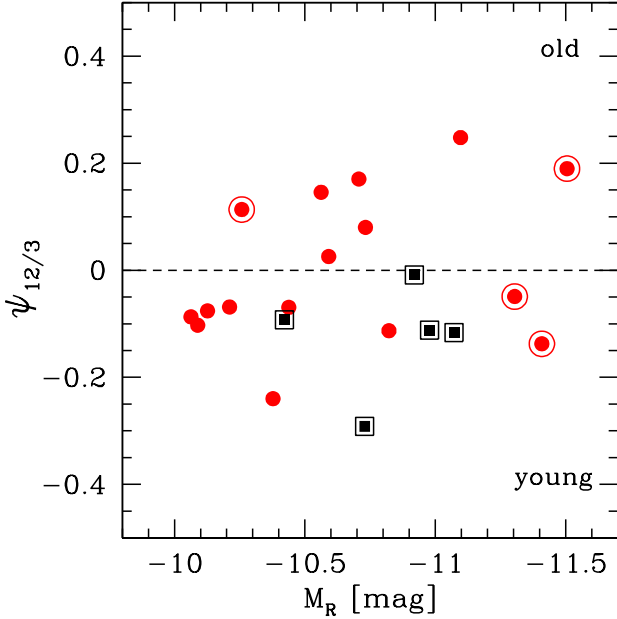


Fig. 9. Absolute magnitude of confirmed cluster members (HCG 22 are filled red circles, HCG 90 are black squares) vs. the ratio between the cross-correlation amplitude using our reference old stellar template and an intermediate age template (3 Gyrs, $[\text{Fe}/\text{H}] = -0.5$ dex; Coelho et al. 2007). Negative to positive values indicate spectra better fit by young to old ages, respectively. Objects marked are the ones with cross-correlation confidence level higher than 5.

magnitude range investigated by us to get an idea how many GCs we should expect to detect. The GCLF of NGC 1199 can be described by a Gaussian with a turnover magnitude of $M_V = -7.33$ and a dispersion of $\sigma = 1.40$ (Harris 2001), and the whole GCS has an estimated total number of objects of 314 ± 105 . With our survey we probe about 6.7% of the GCLF and that corresponds to 16 ± 4 objects in the observed area. This matches the number of 16 compact stellar systems we have detected (21 if corrected for incompleteness) in HCG 22. Hence, we do not detect an overabundance of bright compact objects with respect to an extrapolated GCLF. The magnitude of the brightest UCD detected in either group ($M_V \approx -11$ mag) is typical for the luminosity of the brightest compact object found in galaxies that fall in the same luminosity range $-21 \lesssim M_V \lesssim -20$ mag as the ones investigated here (Hilker et al. 2008). In the Local Group, GCs/UCDs brighter than $M_V = -9.5$ (approximately the faint limit for our sample) are of comparable abundance to that found in the two HCGs: there are two objects in the Galaxy (Harris 1996) and between five and ten objects in M31 (Barmby et al. 2000) depending on the distance modulus adopted. Even though the studied groups are about twice as large as the Local Group, given the uncertainties, the number of bright GCs/UCDs is of the same order.

The abundance of “alpha elements” ($[\alpha/\text{Fe}]$) is an indicator of the star formation time scales and can help to distinguish between different formation channels of UCDs. GCs, on average, have super-solar $[\alpha/\text{Fe}]$, being “alpha enhanced” (Puzia et al. 2006; Colucci et al. 2009; Woodley et al. 2010; Taylor et al. 2010), reflecting their short formation time-scales. UCDs present a broader range of $[\alpha/\text{Fe}]$ abundances

which varies as a function of environment (Mieske et al. 2007; Hau et al. 2009). In Figure 8 it is shown that from our eight UCDs with Lick index measurements, one in each HCG presents slightly sub-solar $[\alpha/\text{Fe}]$ abundances. Five further objects (three in HCG 22 and two in HCG 90) show super-solar abundance, and one object HCG22_UCD001 has solar abundance. Interestingly, the one UCD in HCG 22 with sub-solar abundance is HCG22_UCD002 is the largest UCD ($r_h \approx 21$ pc) and the only one with a spectroscopic age estimate clearly below 12 Gyr. This is consistent with a scenario where this object has been able to form stars over a prolonged period of time until only a few Gyrs ago. Among all compact objects detected, the properties of HCG22_UCD002 differ most from those of normal GCs.

4.3. UCD formation

The formation channels discussed for UCDs can be broken down in two distinct concepts:

- UCDs are the tidally stripped remnants of extended dwarf galaxies, hence of galactic origin and tracing the tidal disruption of low-mass cosmological substructures.
- UCDs were formed together with the main body of their host galaxies’ star cluster system, representing the very bright tail of the globular cluster luminosity function (Mieske et al. 2004; Gregg et al. 2009). This encompasses both the formation of metal-rich UCDs in galaxy mergers (Ashman & Zepf 1992) – possibly as clusters of star clusters (Fellhauer & Kroupa 2002) – and the ‘primordial’ channel (Drinkwater et al. 2004) for the formation of metal-poor compact objects.

Regarding simple number counts, a star-cluster origin for most of the detected UCDs is consistent with our results: the extrapolation of the HCG 22 GCLF to bright luminosities agrees with the number of UCDs. Also their centrally concentrated spatial distribution fits to this scenario.

To better distinguish between the star cluster and galactic origin of UCDs, stellar populations are the key. (Merged) star clusters should likely have simple and single stellar populations, corresponding to the individual clusters out of which they merged, which likely all formed in the same giant molecular cloud. Moreover, they should have short star formation time-scales and therefore be enhanced in α elements. In contrast, compact objects that formed within a deeper dwarf galaxy potential are more prone to prolonged and multiple star formation episodes, e.g. due to gas-infall. Our results indicate a broad range of $[\alpha/\text{Fe}]$ abundances for the UCDs detected covering sub-solar to well super-solar values. One UCD candidate in each group appears to have sub-solar alpha abundances, such that these two are the most promising stripped dwarf galaxy candidates. This especially holds for the HCG 22 UCD, which in addition to the alpha decrement has evidence for intermediate age stellar populations and is comparably large $r_h \sim 21$ pc. Supporting this scenario, the faint end of the luminosity function of galaxies in compact groups is known to be underpopulated (Hunsberger et al. 1998; Mendes de Oliveira & Bolte 1999).

Focusing specifically on the creation of UCDs in galaxy mergers, HCG 90 has an interaction process happening between the three galaxies in our targeted region, HCG 90b, c and d, with evidences of exchange of gas and gas disks with overlapping rotation curves (Plana et al. 1998; Castañeda & Hilker 2004). This likely has originated the IGL component, could have

formed young star clusters, and also distributed pre-existing objects into the IGM. Our results imply that there is a relatively low number of UCDs in HCG 90 in the age range of 0.5 Gyr and older, and that they are most consistent with ages of around a Hubble time. We can thus conclude that before the very last 1-2 galaxy passages, no significant population of UCDs was formed in HCG 90. We are not sensitive to very young objects created after this. Hence, for HCG 90 our results are not sufficiently conclusive to support or disfavour the merger scenario. HCG 22 does not present clear signs of ongoing interaction. However, NGC 1199 presents a central dust lane in its center similar to the more local case of NGC 5128 (CenA) of approximately 3 kpc and about $10^7 M_{\odot}$ (Nieto 1983; Sparks et al. 1985; Veron-Cetty & Veron 1988; Finkelman et al. 2010). This is a quite strong indication of a gas-rich merger, old enough to have settled in a single remnant, that likely has triggered the formation of star clusters. The specific frequency of UCDs in HCG 22 appears to be a few times higher than in HCG 90, which is hence consistent with a scenario where the UCD population in HCG 22 was enhanced by this merger episode.

We conclude that the UCD population detected in each group does in their majority not originate from relatively recent galaxy interactions, but that rather most of the detected UCDs have been brought into the group together with their host galaxies. While the analysis of the objects in HCG 90 seem to favor a formation model where the main process happens on the group potential, the results for HCG 22 seem to favor models where the UCDs are formed in processes happening in the galaxy potential, either primordial or merger induced.

This and the existence of at least 1-2 massive and large UCDs with intermediate ages points to the origin of UCDs being associated to different formation processes and not a universal one.

Future investigations in this context should focus on the search for very young UCD progenitors (few 100 Myrs) by targeting HCGs with small crossing time scales and extending the search to bluer colours.

Acknowledgements. We thank the referee Prof. Michael Drinkwater for his comments. CDR would like to thank the Núcleo de Astrofísica Teórica at the Universidade Cruzeiro do Sul for their hospitality, and the support from the Deutsches Zentrum für Luft- und Raumfahrt, DLR (project number 50 OR 0602) and from the Deutsche Forschungsgemeinschaft, DFG (project number ZI 663/8-1) within the Priority Program 1177 (SPP/DFG). IG is thankful for the financial support through DFG-Projekt BO-779/32-1.

References

- Anders, P. & Fritze-v. Alvensleben, U. 2003, *A&A*, 401, 1063
 Anderson, J. & King, I. R. 2000, *PASP*, 112, 1360
 Anderson, J. & King, I. R. 2006, *PSFs, Photometry, and Astronomy for the ACS/WFC*, Tech. rep.
 Anderson, J., King, I. R., Richer, H. B., et al. 2008, *AJ*, 135, 2114
 Appenzeller, I., Fricke, K., Fürtig, W., et al. 1998, *The Messenger*, 94, 1
 Ashman, K. M. & Zepf, S. E. 1992, *ApJ*, 384, 50
 Barmby, P., Huchra, J. P., Brodie, J. P., et al. 2000, *AJ*, 119, 727
 Bedin, L. R., Cassisi, S., Castellì, F., et al. 2005, *MNRAS*, 357, 1038
 Bekki, K., Couch, W. J., Drinkwater, M. J., & Shioya, Y. 2003, *MNRAS*, 344, 399
 Blakeslee, J. P., Lucey, J. R., Barris, B. J., Hudson, M. J., & Tonry, J. L. 2001, *MNRAS*, 327, 1004
 Bruzual, G. & Charlot, S. 2003, *MNRAS*, 344, 1000
 Cardelli, J. A., Clayton, G. C., & Mathis, J. S. 1989, *ApJ*, 345, 245
 Castañeda, L. & Hilker, M. 2004, *Astronomische Nachrichten Supplement*, 325, 129
 Chiaberge, M., Lim, P. L., Kozhurina-Platais, V., Sirianni, M., & Mack, J. 2009, Updated CTE photometric correction for WFC and HRC, Tech. rep.
 Coelho, P., Bruzual, G., Charlot, S., et al. 2007, *MNRAS*, 382, 498
 Colucci, J. E., Bernstein, R. A., Cameron, S., McWilliam, A., & Cohen, J. G. 2009, *ApJ*, 704, 385
 Da Rocha, C. & Mendes de Oliveira, C. 2005, *MNRAS*, 364, 1069
 Da Rocha, C., Mendes de Oliveira, C., Bolte, M., Ziegler, B. L., & Puzia, T. H. 2002, *AJ*, 123, 690
 Da Rocha, C., Mendes de Oliveira, C., Bolte, M., Ziegler, B. L., & Puzia, T. H. 2003, in *Extragalactic Globular Cluster Systems*, ed. M. Kissler-Patig, 179
 Da Rocha, C., Ziegler, B. L., & Mendes de Oliveira, C. 2008, *MNRAS*, 388, 1433
 Dabringhausen, J., Hilker, M., & Kroupa, P. 2008, *MNRAS*, 386, 864
 Danese, L., de Zotti, G., & di Tullio, G. 1980, *A&A*, 82, 322
 de Carvalho, R. R., Ribeiro, A. L. B., Capelato, H. V., & Zepf, S. E. 1997, *ApJS*, 110, 1
 Dolphin, A. E. 2009, *PASP*, 121, 655
 Drinkwater, M. J., Gregg, M. D., Couch, W. J., et al. 2004, *Publications of the Astronomical Society of Australia*, 21, 375
 Drinkwater, M. J., Jones, J. B., Gregg, M. D., & Phillipps, S. 2000, *Publications of the Astronomical Society of Australia*, 17, 227
 Evstigneeva, E. A., Drinkwater, M. J., Jurek, R., et al. 2007a, *MNRAS*, 378, 1036
 Evstigneeva, E. A., Gregg, M. D., Drinkwater, M. J., & Hilker, M. 2007b, *AJ*, 133, 1722
 Fellhauer, M. & Kroupa, P. 2002, *MNRAS*, 330, 642
 Finkelman, I., Brosch, N., José G. Funes S., J., Kniazev, A. Y., & Väisänen, P. 2010, *ArXiv e-prints*
 Forbes, D. A., Lasky, P., Graham, A. W., & Spitler, L. 2008, *MNRAS*, 389, 1924
 Fruchter, A. S. & Hook, R. N. 2002, *PASP*, 114, 144
 Fujita, Y. 2004, *PASJ*, 56, 29
 Georgiev, I. Y., Goudfrooij, P., Puzia, T. H., & Hilker, M. 2008, *AJ*, 135, 1858
 Gilmore, G., Wilkinson, M. I., Wyse, R. F. G., et al. 2007, *ApJ*, 663, 948
 Goerdt, T., Moore, B., Kazantzidis, S., et al. 2008, *MNRAS*, 385, 2136
 Gregg, M. D., Drinkwater, M. J., Evstigneeva, E., et al. 2009, *AJ*, 137, 498
 Haşegan, M., Jordán, A., Côté, P., et al. 2005, *ApJ*, 627, 203
 Harris, W. E. 1996, *AJ*, 112, 1487
 Harris, W. E. 2001, *Globular cluster systems*, ed. L. Labhardt & B. Binggeli, 223
 Hau, G. K. T., Spitler, L. R., Forbes, D. A., et al. 2009, *MNRAS*, 394, L97
 Hickson, P. 1982, *ApJ*, 255, 382
 Hickson, P., Kindl, E., & Auman, J. R. 1989, *ApJS*, 70, 687
 Hickson, P., Mendes de Oliveira, C., Huchra, J. P., & Palumbo, G. G. 1992, *ApJ*, 399, 353
 Hilker, M., Baumgardt, H., Infante, L., et al. 2007, *A&A*, 463, 119
 Hilker, M., Infante, L., & Richtler, T. 1999, *A&AS*, 138, 55
 Hilker, M., Mieske, S., Baumgardt, H., & Dabringhausen, J. 2008, in *IAU Symposium*, Vol. 246, *IAU Symposium*, ed. E. Vesperini, M. Giersz, & A. Sills, 427–428
 Hunsberger, S. D., Charlton, J. C., & Zaritsky, D. 1998, *ApJ*, 505, 536
 Iglesias-Páramo, J. & Vílchez, J. M. 2001, *ApJ*, 550, 204
 Jones, J. B., Drinkwater, M. J., Jurek, R., et al. 2006, *AJ*, 131, 312
 Kotulla, R., Fritze, U., Weilbacher, P., & Anders, P. 2009, *MNRAS*, 396, 462
 Krist, J. 1995, in *Astronomical Society of the Pacific Conference Series*, Vol. 77, *Astronomical Data Analysis Software and Systems IV*, ed. R. A. Shaw, H. E. Payne, & J. J. E. Hayes, 349
 Kruijssen, J. M. D. & Mieske, S. 2009, *A&A*, 500, 785
 Larsen, S. S. 1999, *A&AS*, 139, 393
 Mendes de Oliveira, C. & Bolte, M. 1999, in *Astronomical Society of the Pacific Conference Series*, Vol. 176, *Observational Cosmology: The Development of Galaxy Systems*, ed. G. Giuricin, M. Mezzetti, & P. Salucci, 122
 Mendes de Oliveira, C. & Hickson, P. 1994, *ApJ*, 427, 684
 Mendes de Oliveira, C., Plana, H., Amram, P., Balkowski, C., & Bolte, M. 2001, *AJ*, 121, 2524
 Mieske, S., Hilker, M., & Infante, L. 2002, *A&A*, 383, 823
 Mieske, S., Hilker, M., & Infante, L. 2004, *A&A*, 418, 445
 Mieske, S., Hilker, M., Jordán, A., Infante, L., & Kissler-Patig, M. 2007, *A&A*, 472, 111
 Mieske, S., Hilker, M., Jordán, A., et al. 2008, *A&A*, 487, 921
 Mieske, S. & Kroupa, P. 2008, *ApJ*, 677, 276
 Misgeld, I., Hilker, M., & Mieske, S. 2009, *A&A*, 496, 683
 Misgeld, I., Mieske, S., & Hilker, M. 2008, *A&A*, 486, 697
 Mulchaey, J. S. & Zabludoff, A. I. 1998, *ApJ*, 496, 73
 Nieto, J. L. 1983, in *Astrophysics and Space Science Library*, Vol. 103, *Astrophysical Jets*, ed. A. Ferrari & A. G. Pacholczyk, 113–130
 Osmond, J. P. F. & Ponman, T. J. 2004, *MNRAS*, 350, 1511
 Plana, H., Mendes de Oliveira, C., Amram, P., & Boulesteix, J. 1998, *AJ*, 116, 2123
 Ponman, T. J., Bourner, P. D. J., Ebeling, H., & Bohringer, H. 1996, *MNRAS*, 283, 690
 Prugniel, P. & Simien, F. 1996, *A&A*, 309, 749
 Puzia, T. H., Kissler-Patig, M., & Goudfrooij, P. 2006, *ApJ*, 648, 383
 Puzia, T. H., Saglia, R. P., Kissler-Patig, M., et al. 2002, *A&A*, 395, 45
 Ribeiro, A. L. B., de Carvalho, R. R., Capelato, H. V., & Zepf, S. E. 1998, *ApJ*,

497, 72

- Rudick, C. S., Mihos, J. C., & McBride, C. 2006, *ApJ*, 648, 936
- Schlegel, D. J., Finkbeiner, D. P., & Davis, M. 1998, *ApJ*, 500, 525
- Schuberth, Y., Richtler, T., Hilker, M., et al. 2009, ArXiv e-prints
- Sirianni, M., Jee, M. J., Benítez, N., et al. 2005, *PASP*, 117, 1049
- Sparks, W. B., Wall, J. V., Thorne, D. J., et al. 1985, *MNRAS*, 217, 87
- Taylor, M. A., Puzia, T. H., Harris, G. L., et al. 2010, *ApJ*, 712, 1191
- Thomas, D., Maraston, C., & Bender, R. 2003, *MNRAS*, 339, 897
- Trager, S. C., Worthey, G., Faber, S. M., Burstein, D., & Gonzalez, J. J. 1998, *ApJS*, 116, 1
- Treister, E., Castander, F. J., Maccarone, T. J., et al. 2005, *ApJ*, 621, 104
- Tzanavaris, P., Hornschemeier, A. E., Gallagher, S. C., et al. 2010, *ApJ*, 716, 556
- van Dokkum, P. G. 2001, *PASP*, 113, 1420
- Verdes-Montenegro, L., Yun, M. S., Williams, B. A., et al. 2001, *A&A*, 377, 812
- Veron-Cetty, M.-P. & Veron, P. 1988, *A&A*, 204, 28
- White, N. E., Giommi, P., & Angelini, L. 2000, *VizieR Online Data Catalog*, 9031, 0
- White, P. M., Bothun, G., Guerrero, M. A., West, M. J., & Barkhouse, W. A. 2003, *ApJ*, 585, 739
- Woodley, K. A., Harris, W. E., Puzia, T. H., et al. 2010, *ApJ*, 708, 1335
- Worthey, G. 1994, *ApJS*, 95, 107
- Zabludoff, A. I. & Mulchaey, J. S. 1998, *ApJ*, 496, 39

Table 1. Properties of the 16 compact stellar systems detected in HCG 22, ordered by R -band magnitude. The fifth column gives the confidence level R of the cross-correlation radial velocity measurement, performed with the IRAF task `fxcor`. The last column gives a metallicity estimate for those sources with high enough S/N, i.e. an error of less than 0.5 dex.

ID	RA	DEC	v_{rad} [km s $^{-1}$]	R	H_{β} [Å]	Mgb [Å]	$\langle\text{Fe}\rangle$ [Å]	[Fe/H] [dex]
HCG22_UCD001	03 ^h 03 ^m 34 ^s .46	−15°36′45″.8	2834 ± 27	12.7	0.62 ± 0.96	2.97 ± 0.97	2.40 ± 0.70	−0.3 ± 0.3
HCG22_UCD002	03 ^h 03 ^m 36 ^s .24	−15°37′12″.8	2552 ± 78	5.1	3.22 ± 0.98	1.31 ± 1.04	2.18 ± 0.81	−0.8 ± 0.5
HCG22_UCD003	03 ^h 03 ^m 43 ^s .94	−15°37′13″.0	2652 ± 92	4.6				
HCG22_UCD004	03 ^h 03 ^m 44 ^s .62	−15°37′43″.4	2668 ± 70	7.9	2.23 ± 1.47	5.91 ± 1.42	2.67 ± 1.03	0.1 ± 0.3
HCG22_UCD005	03 ^h 03 ^m 40 ^s .79	−15°36′57″.1	2665 ± 51	8.5	1.44 ± 1.06	3.10 ± 1.03	1.59 ± 0.84	−0.5 ± 0.4
HCG22_UCD006	03 ^h 03 ^m 40 ^s .74	−15°37′25″.5	2654 ± 118	4.8				
HCG22_UCD007	03 ^h 03 ^m 34 ^s .24	−15°37′03″.2	2548 ± 218	4.0				
HCG22_UCD008	03 ^h 03 ^m 35 ^s .04	−15°37′30″.9	2944 ± 70	4.4				
HCG22_UCD009	03 ^h 03 ^m 39 ^s .55	−15°37′37″.8	2211 ± 74	5.9				
HCG22_UCD010	03 ^h 03 ^m 32 ^s .66	−15°38′29″.0	2755 ± 264	2.9				
HCG22_UCD011	03 ^h 03 ^m 30 ^s .09	−15°38′09″.0	2766 ± 95	4.3*				
HCG22_UCD012	03 ^h 03 ^m 36 ^s .32	−15°37′15″.8	2549 ± 35	10.1	2.65 ± 1.62	7.53 ± 1.50	4.03 ± 1.18	0.4 ± 0.2
HCG22_UCD013	03 ^h 03 ^m 44 ^s .93	−15°36′54″.7	2646 ± 100	3.2				
HCG22_UCD014	03 ^h 03 ^m 40 ^s .55	−15°36′18″.7	2905 ± 114	2.8				
HCG22_UCD015	03 ^h 03 ^m 40 ^s .18	−15°37′00″.9	2789 ± 60	2.7				
HCG22_UCD016	03 ^h 03 ^m 38 ^s .07	−15°37′18″.6	2487 ± 128	3.1				

* Cross correlation amplitude using an alternative intermediate age template (see text for details).

Table 2. Properties of the 5 compact stellar systems detected in HCG 90, ordered by R -band magnitude. The fifth column gives the confidence level R of the cross-correlation radial velocity measurement, performed with the IRAF task `fxcor`. The last column gives a metallicity estimate for those sources with high enough S/N, i.e. an error of less than 0.5 dex.

ID	RA	DEC	v_{rad} [km s $^{-1}$]	R	H_{β} [Å]	Mgb [Å]	$\langle\text{Fe}\rangle$ [Å]	[Fe/H]
HCG90_UCD001	22 ^h 01 ^m 57 ^s .99	−31°57′31″.9	2911 ± 34	11.8	2.14 ± 0.62	3.62 ± 0.63	1.46 ± 0.51	−0.5 ± 0.2
HCG90_UCD002	22 ^h 01 ^m 56 ^s .59	−31°59′25″.3	2567 ± 41	9.2	1.80 ± 0.61	1.24 ± 0.65	2.05 ± 0.50	−0.9 ± 0.3
HCG90_UCD003	22 ^h 01 ^m 56 ^s .42	−31°57′15″.5	2536 ± 35	11.5	2.34 ± 0.77	2.85 ± 0.81	1.36 ± 0.63	−0.6 ± 0.3
HCG90_UCD004	22 ^h 02 ^m 01 ^s .41	−31°55′60″.0	2423 ± 73	5.5				
HCG90_UCD005	22 ^h 02 ^m 00 ^s .83	−31°58′26″.7	3237 ± 65	5.6				

Table 3. Photometric and structural properties of HCG 22 UCD candidates from the HST imaging. The columns list the object ID, foreground reddening corrected ACS Vega and ground based Johnson/Cousins magnitudes, half-light radius in pixels and in parsecs calculated with $DM = 32.6$ mag, King concentration parameter and the S/N of the source detection.

ID	F450W ₀ [mag]	F606W ₀ [mag]	F814W ₀ [mag]	B_0 [mag]	R_0 [mag]	r_h [pix]	r_h [pc]	r_i/r_c	S/N
HCG22_UCD001	21.926 ± 0.108	20.742 ± 0.083	19.783 ± 0.092	22.56	21.10	0.63 ^{+0.013} _{−0.021}	10.11	30	72.9
HCG22_UCD002	21.767 ± 0.150	20.853 ± 0.129	20.127 ± 0.138	22.31	21.19	1.29 ^{+0.047} _{−0.046}	20.71	15	56.4
HCG22_UCD003	–	–	–	22.46	21.30	–	–	–	–
HCG22_UCD004	–	–	–	23.10	21.50	–	–	–	–
HCG22_UCD005	22.244 ± 0.064	21.362 ± 0.051	20.477 ± 0.083	22.91	21.78	0.11 ^{+0.055} _{−0.016}	1.77	5	46.0
HCG22_UCD006	–	–	–	23.17	21.87	–	–	–	–
HCG22_UCD007	22.470 ± 0.078	21.647 ± 0.072	20.797 ± 0.085	23.21	21.89	0.43 ^{+0.032} _{−0.025}	6.90	5	42.8
HCG22_UCD008	22.601 ± 0.083	21.778 ± 0.057	20.997 ± 0.075	23.19	22.01	0.55 ^{+0.037} _{−0.053}	8.83	5	34.6
HCG22_UCD009	–	–	–	23.48	22.04	–	–	–	–
HCG22_UCD010	–	–	–	23.29	22.16	–	–	–	–
HCG22_UCD011	23.079 ± 0.074	22.038 ± 0.071	21.292 ± 0.088	23.35	22.22	0.31 ^{+0.063} _{−0.036}	4.98	5	30.4
HCG22_UCD012	22.972 ± 0.085	21.919 ± 0.052	20.897 ± 0.061	23.83	22.34	0.44 ^{+0.032} _{−0.055}	7.06	5	27.3
HCG22_UCD013	–	–	–	23.77	22.39	–	–	–	–
HCG22_UCD014	22.938 ± 0.079	22.018 ± 0.052	21.220 ± 0.095	23.57	22.47	0.19 ^{+0.164} _{−0.024}	3.05	30	28.4
HCG22_UCD015	22.994 ± 0.078	22.088 ± 0.056	21.218 ± 0.101	23.80	22.51	0.40 ^{+0.204} _{−0.121}	6.42	5	24.6
HCG22_UCD016	23.025 ± 0.098	22.118 ± 0.080	21.450 ± 0.106	23.59	22.54	0.28 ^{+0.139} _{−0.046}	4.50	5	22.4

Table 4. Photometric and structural properties of HCG 90 UCD candidates from the HST imaging. The columns list the object ID, foreground reddening corrected WFPC2 Vega and ground based Johnson/Cousins magnitudes, half-light radius in pixels and in parsecs calculated with $DM = 32.6$ mag, King concentration parameter and the S/N of the source detection.

ID	F475W ₀ [mag]	F850LP ₀ [mag]	B ₀ [mag]	V ₀ [mag]	R ₀ [mag]	r _h [pix]	r _h [pc]	r _t /r _c	S/N
HCG90_UCD001	–	–	22.96	22.00	21.53	–	–	–	–
HCG90_UCD002	–	–	22.93	22.07	21.62	–	–	–	–
HCG90_UCD003	–	–	22.91	22.10	21.68	–	–	–	–
HCG90_UCD004	–	–	23.05	22.26	21.87	–	–	–	–
HCG90_UCD005	22.978 ± 0.026	21.359 ± 0.145	23.45	22.61	22.18	0.39 ^{+0.016} _{-0.001}	3.13	100	0.21 ^{+0.035} _{-0.104}

**Appendix A: High resolution colour view of our
observed fields**

Fig. A.1. Colour composite image of HCG 22 with Keck *B* and *R*-band (Da Rocha et al. 2002) and HST/WFPC2 F450W, F606W and F814W filters. A zoom in ($20 \times 20''$) showing the dust lane in NGC 1199 can be seen in the upper left corner. As in Figure 1, blue diamonds indicate the targeted objects in our masks and red circles indicate the HCG compact members. Field of view is $7 \times 5'$.

Fig. A.2. Colour composite image of HCG 90 with FORS *B*, *V* and *R*-band and HST/ACS F475W and F850LP filters. A zoom in ($38.5 \times 57.7''$) showing the interacting pair NGC 7174/7176 can be seen in the upper right corner. As in Figure 1, blue diamonds indicate the targeted objects in our masks and red circles indicate the HCG compact members detected. Field of view is $7 \times 7'$.

This figure "ucdhcg_fig_h22_colour.jpg" is available in "jpg" format from:

<http://arxiv.org/ps/1009.3010v1>

This figure "ucdhcg_fig_h90_colour.jpg" is available in "jpg" format from:

<http://arxiv.org/ps/1009.3010v1>